



Small effect of water incorporation on dislocation mobility in olivine: Negligible creep enhancement and water-induced fabric transition in the asthenosphere



Lin Wang^a, Artem Chanyshv^{a,b,*}, Nobuyoshi Miyajima^a, Takaaki Kawazoe^c,
Stephan Blaha^a, Jia Chang^{a,d}, Tomoo Katsura^a

^a Bayerisches Geoinstitut, University of Bayreuth, 95440 Bayreuth, Germany

^b Deutsches Elektronen-Synchrotron DESY, Notkestr. 85, 22607 Hamburg, Germany

^c Department of Earth and Planetary Systems Science, Hiroshima University, 739-8526 Higashi-Hiroshima, Japan

^d State Key Laboratory of Geological Processes and Mineral Resources and Faculty of Earth Resources, China University of Geosciences, Wuhan 430074, China

ARTICLE INFO

Article history:

Received 7 July 2021

Received in revised form 20 December 2021

Accepted 25 December 2021

Available online 13 January 2022

Editor: J. Badro

Keywords:

water
upper mantle viscosity
olivine fabric transition

ABSTRACT

To constrain the effect of water on upper mantle dynamics, we measured the annihilation rate coefficients (k) of [100](010) and [001](100) dislocations in olivine, referred to as a -dislocations and c -dislocations, respectively, as a function of water content. Natural olivine single crystals were doped with 5–800 wt. ppm water and sheared in the [100] or [001] directions along the (010) and (100) planes to produce a - and c -dislocations, respectively, and then annealed under quasi-hydrostatic conditions at a constant pressure and temperature of 5 GPa and 1473 K. The obtained annihilation rate coefficients are fitted to a power-law equation, yielding astonishingly small water-content exponents of 0.0 ± 0.1 and 0.2 ± 0.2 for the a - and c -dislocations, respectively. The overall effect of water on dislocation mobility is therefore small because these two slip systems are considered to be the least and most sensitive to water, respectively. These results imply that water incorporation does not effectively increase the dislocation-creep rate and that a water-induced fabric transition is unlikely. The effects of water on asthenospheric dynamics may thus be limited, and the lateral seismic anisotropy changes observed in the asthenosphere may solely reflect changes of mantle flow geometry.

© 2021 The Author(s). Published by Elsevier B.V. This is an open access article under the CC BY-NC-ND license (<http://creativecommons.org/licenses/by-nc-nd/4.0/>).

1. Introduction

The water incorporation into olivine, namely the incorporation of H into the olivine crystal structure, is expected to affect asthenospheric dynamics. Strong seismic anisotropy in the oceanic asthenosphere (Ekström and Dziewonski, 1998; Gaherty, 2001; Gung et al., 2003; Montagner and Guillot, 2002; Visser et al., 2008) indicates that the dislocation creep of olivine plays an essential role in upper-mantle rheology. Early deformation experiments (Chopra and Paterson, 1984; Karato and Jung, 2003; Karato et al., 1986; Mei and Kohlstedt, 2000) suggested that water incorporation strongly enhances olivine dislocation creep, which could introduce a strong viscosity contrast between the asthenosphere and lithosphere (Hirth and Kohlstedt, 2003; Kohlstedt, 2006). In addition to creep enhancement, water incorporation has also been

considered to alter the olivine fabric, namely the lattice preferred orientation (LPO) that forms in response to deformation (Jung and Karato, 2001; Katayama et al., 2004; Masuti et al., 2019), which reflects the differing water-content dependences of dislocation mobility in different slip systems. A water-induced fabric transition modifies the interpretation of mantle flow patterns and estimates of the water distribution in the asthenosphere based on seismic anisotropy (Karato and Jung, 2003; Karato et al., 2008).

However, the application of experimental deformation results to the asthenosphere requires careful justification. Although the high applied stresses in deformation experiments are comparable with those at the upper interface of subducting slabs, they are many orders of magnitude higher than those in the oceanic asthenosphere. Such a colossal difference may alter the mechanism of dislocation motion (Cordier et al., 2012). The majority of hydrous deformation experiments were also conducted under water-saturated conditions (Chopra and Paterson, 1984; Karato and Jung, 2003; Karato et al., 1986; Mei and Kohlstedt, 2000), which are dissimilar to the majority of the asthenosphere, where the water content in olivine

* Corresponding author at: Bayerisches Geoinstitut, University of Bayreuth, 95440 Bayreuth, Germany.

E-mail address: artem.chanyshv@uni-bayreuth.de (A. Chanyshv).

ranges from only 20 to 300 wt. ppm (Dixon et al., 2004; Li et al., 2008). Another problem with water saturation is that the olivine water contents and confining pressure cannot be independently controlled. Previous studies therefore could not separate the water effect from the pressure effect, which is poorly understood.

In contrast to the results reported from deformation experiments, measurements of Si and O diffusion rates in olivine, which have been proposed to control dislocation creep under low-stress conditions, showed a small effect of water incorporation (Fei et al., 2013, 2014). These results imply that an increase in water content by a factor of 10 may only enhance the dislocation creep rate by a factor of two. Water incorporation has also been shown to not enhance Si and O diffusion rates in a particular crystallographic orientation (Costa and Chakraborty, 2008), which implies that the dislocation mobility in different slip systems should have similar water-content dependences. A water-induced fabric transition is therefore unlikely. However, the dislocation creep rates evaluated using Si and O diffusivity data are based on the assumption that the diffusive motion of atoms purely controls dislocation creep. This rough assumption hinders any definitive conclusion regarding water effects on the dislocation creep rate and fabric transition. Diffusion experiments are also conducted using essentially dislocation-free crystals, which prevents a direct study of dislocation creep.

For these reasons, the effect of water on olivine dislocation creep must be examined using a method that is independent of deformation and diffusion techniques. In this study, we adopted the dislocation recovery method (Kohlstedt et al., 1980; Toriumi and Karato, 1978) to study the effect of water on olivine dislocation mobility in different slip systems.

Samples with pre-activated dislocations were annealed under the target conditions. During annealing, two dislocations with different signs annihilate. Therefore, the recovery kinetics is second order (Farla et al., 2011; Karato and Ogawa, 1982; Kohlstedt et al., 1980; Toriumi and Karato, 1978):

$$\frac{d\rho}{dt} = -k\rho^2, \quad (1)$$

where ρ and t are the dislocation density and annealing time, respectively, and k is a rate coefficient that depends on the temperature, pressure, and water content. Because k is proportional to dislocation mobility (Karato and Ogawa, 1982), their water-content dependences are identical. An advantage of this method compared with deformation experiments is that the obtained water-content dependence is relevant to deformation under low-stress and water-undersaturated conditions typical of the asthenosphere. Dislocation annihilation is rate-limited by climb motion, which controls the dislocation velocity under low-stress conditions (Kohlstedt, 2006). Although dislocation motion is driven by internal stresses in dislocation recovery experiments, compared with external stresses in bulk deformation experiments, the mechanisms of dislocation motion under internal and external stresses are identical. Furthermore, because the samples are annealed under hydrostatic conditions, the water content can be controlled below the water solubility of olivine, which is appropriate for the majority of the asthenosphere, where no free water exists. The dislocation-annihilation rates are slip-system specific and can therefore be used to verify a potential fabric transition caused by differing water effects in different slip systems.

This study determined the dislocation-annihilation rates of the [100](010) and [001](100) slip systems, referred to as **a**-slip and **c**-slip, respectively. These slip systems were chosen because Jung and Karato (2001) suggested that **a**- and **c**-slip respectively dominate in the low and high water contents under low-stress conditions, which implies that they are the least and most water-sensitive.

Although Katayama et al. (2004) reported the [100](001) slip system, its occurrence at intermediate water contents indicates the water effect on this slip system is between those of **a**- and **c**-slip. We therefore did not investigate the [100](001) slip system. Some studies have reported another slip system, i.e., the [001](010) slip system. However, because this slip system appears under high-stress conditions above ~400 MPa (Jung and Karato, 2001), it is non-essential for investigating the main parts of the asthenosphere (Sternai et al., 2016).

Deformation experiments on polycrystalline olivine suggested that the strain rate increases proportionally to the power of 1.2 of the water content. We therefore expect that the water-content exponent of the **a**- and **c**-dislocations may be lower and higher than 1.2, respectively. However, in contrast to these expectations, our results demonstrate that the water-content exponents of the **a**- and **c**-dislocations are substantially smaller and identical within error. These results imply that the water enhancement of olivine dislocation creep is minor and that a water-induced olivine fabric transition may not occur in the asthenosphere.

2. Experimental procedure

2.1. Sample preparation

Single crystals of natural olivine from Pakistan were used in this study. Their major and trace element contents were determined by energy dispersive spectroscopy (EDS) and laser-ablation inductively-coupled-plasma mass spectrometry (LA-ICP-MS), respectively. Although Pakistan olivine does not have a mantle origin, its major and minor compositions are similar to those of San Carlos olivine (Gose et al., 2010). The crystallographic orientation of each crystal was determined using a Huber single-crystal diffractometer operated by SINGLE2014 (Angel and Finger, 2011). The oriented olivine crystals were mounted in epoxy resin with the (010) and (100) planes exposed to the surface for the **a**-dislocation and **c**-dislocation experiments, respectively. The samples were polished using diamond powder with a grain size of 0.25 μm . The crystallographic orientations parallel to the exposed planes were determined using electron backscatter diffraction. The oriented crystals were shaped into cubes with a 1.5-mm edge length along their crystallographic planes with less than 5° error.

2.2. Hydration/dehydration

The olivine specimens were hydrated or dehydrated after shaping. In the dehydration experiments, the cubes were placed in a Pt basket and annealed at ambient pressure and a temperature of 1473 K for 12 h in a CO-CO₂ gas-mixing furnace. The oxygen partial pressure was controlled at 10^{-7.5} MPa near the enstatite-magnesite-olivine-graphite (EMOG) buffer.

The hydration experiments were conducted using a Kawai-type multi-anvil apparatus at the Bayerisches Geoinstitut, University of Bayreuth. The cell assembly is shown in Fig. S1. Single-crystal olivine cubes were loaded into gold capsules with outer and inner diameters of 3.7 and 3.2 mm, respectively, with one end sealed. A mixture of talc, brucite, and FeO powders with a weight ratio of 1.7:1.0:0.3 was loaded into the sealed end of the capsules. This mixture served as a water source, controlled the silica activity, and avoided iron loss in the samples. This became an aggregate of (Mg_{0.9}Fe_{0.1})₂SiO₄ and (Mg_{0.9}Fe_{0.1})SiO₃ with a molar ratio of 9:1 after releasing water. The cubes were surrounded by graphite powder to prevent mechanical damage during compression and approximately constrain the oxygen fugacity within the capsules to the EMOG-buffer conditions. The water contents in the samples were controlled by varying the ratios of the water source to graphite. The open ends of the capsules were closed

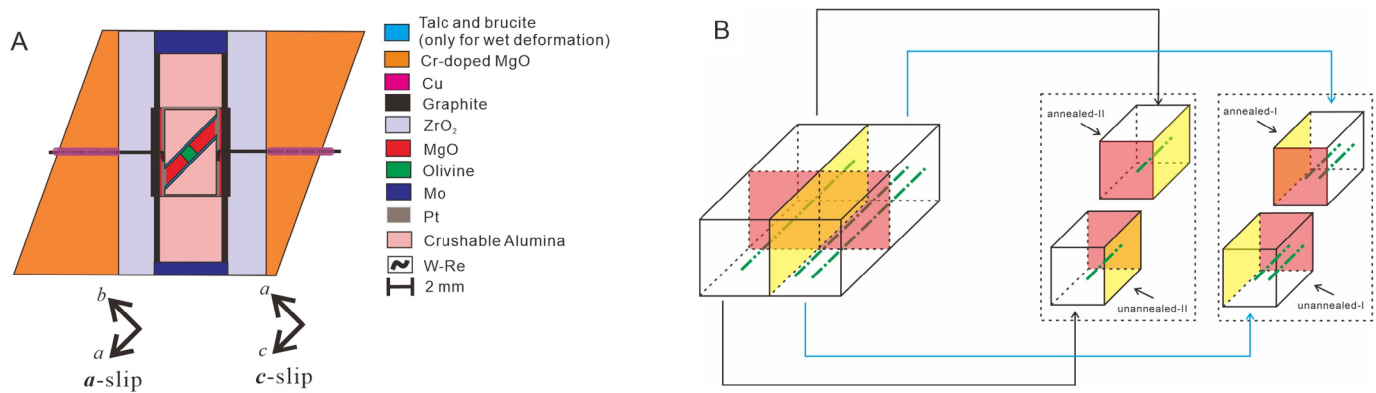


Fig. 1. (A) Sample assembly used in the deformation experiments to activate *a*- and *c*-dislocations. The crystallographic orientation of the olivine single crystal is also shown. (B) Schematic plot of the cutting geometry of a deformed sample. The red and yellow planes indicate the cutting planes. The red cutting plane is perpendicular to the dislocation lines (green dash-dot lines). The pieces that share the red cutting plane are paired in the same group, namely, unannealed-I and annealed-I are paired and unannealed-II and annealed-II are paired. The dislocation density was observed on the red cutting plane in the annealed and unannealed pieces in the same group. (For interpretation of the colors in the figures, the reader is referred to the web version of this article.)

and sealed via arc welding after loading. The capsule was placed in an MgO cylinder in a stepped graphite heater with a ZrO₂ thermal insulator. Tungsten carbide anvils with 15-mm truncated edge lengths were used to generate high pressure together with a Cr₂O₃-doped MgO octahedron with a 25-mm edge length as the pressure medium. The sample pressures were estimated based on a calibration of the hydraulic oil pressure using the phase transitions of Bi at ambient temperature. The temperature was measured using a W97%Re3%–W75%Re25% thermocouple whose junction was near one end of the capsule. The samples were pressurized to 5 GPa in 4 h, heated to 1470 K at a rate of 50 K/min, and maintained at this temperature for more than 12 h. The samples were then quenched by switching off the heating power and decompressed to ambient pressure over 16 h. After hydration, the samples were polished into cubes with edge lengths of 1.0–1.2 mm to remove graphite and magnesite from the sample surfaces.

2.3. Generation of *a*- and *c*-dislocations

Deformation experiments were conducted at 5 GPa and 1470 K using the same Kawai-type multi-anvil apparatus. Fig. 1A shows the experimental setup, which is similar to that used in our previous study (Wang et al., 2016), except for the following three points. First, the olivine crystals were oriented so that their [100] direction on the (010) plane was parallel to the shear direction when activating *a*-dislocations, and their [001] direction on the (100) plane was parallel to the shear direction when activating *c*-dislocations. Second, thin layers of talc + brucite + FeO mixtures were placed between the MgO slices and alumina pistons to prevent olivine dehydration during deformation and a change in the Mg/Fe ratio. Third, the Pt capsules were sealed via welding.

The samples were first pressurized to the target pressure of 5 GPa at ambient temperature over 4 h. The target temperature of 1470 K was reached in 15 min and then maintained for 15 min to sinter the crushable alumina. The samples were then further compressed by increasing the press load by 0.2 MN over 15 min for the deformation. After deformation, the samples were quenched by switching off the heating power and then decompressed to ambient pressure over more than 16 h. A cold compression experiment without heating and additional increase of the oil pressure was also conducted to check whether dislocations can be generated during cold compression.

2.4. TEM observations

Parts of the *c*-deformed samples before annealing were fixed on glass slides and double-side polished parallel to the (100) planes

to thicknesses ranging from 23 to 35 μm . After removing the olivine crystals from the glass slides, the samples were thinned via Ar ion milling with a voltage of 4.5 kV and incident angles of 4°–8° from the top to bottom of the ion bombardment. The total thinning time varied between 14 and 25 h depending on the thickness and size of each sample. Transmission electron microscope (TEM) observations were performed using an FEI Titan G2 80-200 S/TEM with four silicon drift detectors for energy-dispersive X-ray spectroscopy, operating at an acceleration voltage of 200 kV. The dislocation microstructures were examined using dark-field and weak-beam dark-field imaging and selected area electron diffraction. We chose a diffraction vector with $\mathbf{g} = 004$ to observe the [001] dislocations and determine their characteristics.

2.5. Annealing for dislocation annihilation

The deformed single crystals were cut into four pieces and paired into two groups. The two pieces in the same group have the common cutting plane, which was perpendicular to the dislocation lines of the dominant dislocation segments (Fig. 1B). One piece of each pair was used in an annealing experiment, and the other piece was used to determine the dislocation density prior to annealing. The annealing experiments were conducted at 5 GPa and 1473 K using a Kawai-type multi-anvil apparatus. The cell assembly was identical to that used in the hydration experiments.

2.6. Chemical analysis

The compositions of the deformed samples were determined by EDS. The water contents of the samples before and after annealing were determined via unpolarized Fourier-transform infrared spectroscopy (FTIR) with 200 scans for each spectrum at a resolution of 1 cm^{-1} . Spectra were measured at the rims and centers of the samples after annealing to examine the water distribution inside the samples. The light paths were oriented perpendicular to the (010) planes of the samples. The Paterson calibration (Paterson, 1982) was used to calculate the water contents.

2.7. Dislocation-density measurements

Dislocations were observed using the same oxidation decoration technique as in Wang et al. (2016) except for the oxidation temperature, which was 1070 K in this study. Corresponding areas away from the cracks in the initial and annealed pieces from the

Table 1Summary of the experimental conditions and results.¹

No.	Mg#	Water content before (wt. ppm)	Water content after (wt. ppm)	ρ_i (μm^{-2})	Examined areas (μm^2)	ρ_f (μm^{-2})	t (h)	Examined area (μm^2)	Log k ($\text{m}^2 \text{s}^{-1}$)
Z1483 [*] (c)	93.3 ± 0.3	5	5	8.091 ± 0.946	1079	0.463 ± 0.037	18.2	1165	-16.5 ± 0.1
Z1495 [*] (c)	92.3 ± 0.6	5	7	1.312 ± 0.158	2735	0.665 ± 0.045	15.5	2734	-16.9 ± 0.1
Z1495-2 [*] (c)	92.3 ± 0.6	5	7	2.361 ± 0.499	1047	0.512 ± 0.096	15.5	1637	-16.6 ± 0.1
Z1675 [*] (c)	92.3 ± 0.1	19	25	0.329 ± 0.112	2735	0.202 ± 0.053	10	2734	-16.3 ± 0.4
Z1712 [#] (c)	92.2 ± 0.5	86	91	1.914 ± 0.104	1820	0.883 ± 0.095	6	1823	-16.5 ± 0.1
Z1712-2 [#] (c)	92.2 ± 0.5	86	91	1.113 ± 0.141	1820	0.713 ± 0.091	6	1022	-16.6 ± 0.2
Z1731 [#] (c)	92.5 ± 0.6	76	75	2.549 ± 0.055	1165	0.539 ± 0.113	6	1165	-16.2 ± 0.1
Z1924 (a)	91.3 ± 0.1	124	180	0.211 ± 0.057	1631	0.051 ± 0.014	20	1639	-15.7 ± 0.2
Z1940 (a)	90.2 ± 0.2	753	973	0.083 ± 0.003	10160	0.033 ± 0.009	12	7020	-15.4 ± 0.2
Z1940-2 (a)	90.2 ± 0.2	753	973	0.078 ± 0.002	10123	0.028 ± 0.007	12	7040	-15.3 ± 0.2
Z1947 (a)	90.1 ± 0.2	62	38	0.062 ± 0.006	6015	0.023 ± 0.004	16	6780	-15.3 ± 0.2
Z1989 (a)	90.4 ± 0.1	26	13	0.190 ± 0.106	15549	0.115 ± 0.022	4	15562	-15.4 ± 0.2
Z1994 (a)	90.1 ± 0.2	32	22	0.057 ± 0.003	4413	0.022 ± 0.002	20	4366	-15.4 ± 0.1
Z1994-2 (a)	90.1 ± 0.2	32	22	0.047 ± 0.002	4374	0.013 ± 0.002	20	4346	-15.1 ± 0.1

¹ All annealing experiments were conducted at 5 GPa and 1473 K. The a and c in the parentheses represent *a*- and *c*-dislocation experiments, respectively.^{*} Anhydrous annealing experiments, samples from anhydrous deformation experiments.[#] Hydrous annealing experiments, samples from hydrous deformation experiment.

same group were observed to determine the change in dislocation density before and after annealing. Rate coefficient errors caused by the heterogeneous distribution of dislocations were reduced using this group-coupling method (Wang et al., 2016).

2.8. Data reduction

By integrating Eq. (1), k can be expressed as (Karato and Ogawa, 1982; Kohlstedt et al., 1980):

$$k = \frac{\frac{1}{\rho_f} - \frac{1}{\rho_i}}{t}, \quad (2)$$

where ρ_f and ρ_i are the dislocation densities after and before annealing, respectively, and t is the annealing time. The k values at different water contents were fitted to a power-law equation:

$$k = k_0 C_{\text{OH}}^r, \quad (3)$$

where k_0 is a constant, C_{OH} is the water content, and r is the water exponent. As discussed, this exponent represents the water-content dependence of the dislocation creep rate.

3. Experimental results

3.1. Chemical composition

The major and trace elements of the samples before deformation are reported in Table S1. The magnesium numbers of the samples after deformation are reported in Table 1. Fig. 2 shows the FTIR spectra of the samples before and after annealing. Despite annealing, the water contents remained nearly unchanged owing to the same amount of water source in both the hydration and annealing experiments. The spectra measured at the rims and centers of the hydrated annealed samples were identical. According to diffusion theory, the absence of a concentration gradient leads to no change in water content with time. The water contents in the samples were lower than the water solubility of olivine (Kohlstedt et al., 1996), leading to water under-saturated conditions.

3.2. Dislocation structures

Representative SEM images of oxidation-decorated samples with *a*- and *c*-dislocations before and after annealing are shown in Fig. 3. Images of all other samples are shown in Fig. S2 and S3. The TEM observations indicate that the characteristics of the

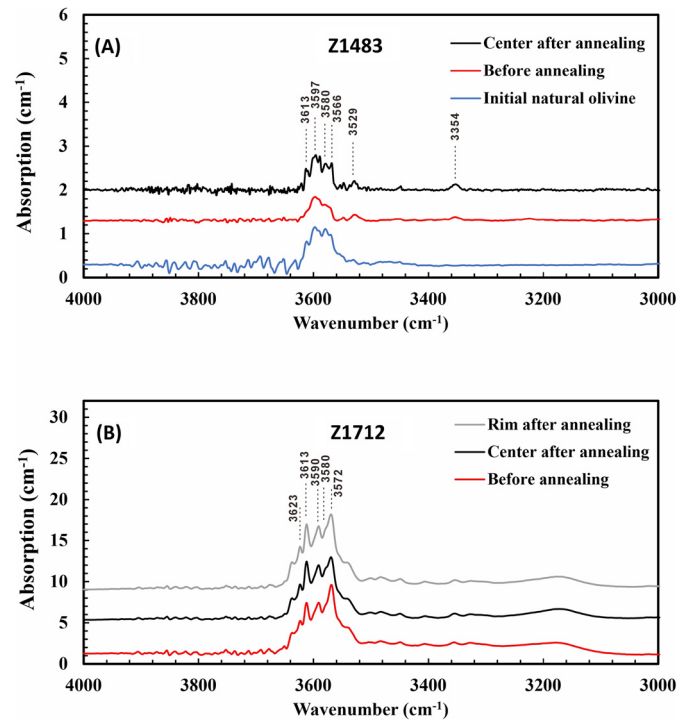


Fig. 2. FTIR spectra after baseline correction and thickness normalization to 1 cm: (A) anhydrous samples and (B) hydrous samples. The black and gray spectra are from annealed samples, whereas the red spectra are from samples before annealing. The blue spectrum in (A) is from the initial natural olivine. The gray and black spectra in (B) are from the rim and center of the annealed sample. Typical OH bands in the spectra are indexed.

dominant *c*-dislocation segments are sensitive to water content. The TEM images show that screw segments of the *c*-dislocations dominate (Fig. 4A) at lower water contents (<25 wt. ppm), which indicates that screw segments slip slower than edge segments in *c*-dislocations. However, the situation reverses at higher water contents where edge segments dominate, as shown in Fig. 4B. This observation indicates that the edge segments slip slower at higher water contents. On the other hand, edge segments are consistently dominant in *a*-dislocations regardless of water content, as demonstrated in previous TEM observations (Girard et al., 2013; Wang et al., 2016). No dislocation line-structure was observed in the oxidation-decorated *a*-slip sample on the (001) plane (Fig. 3, S2) also supported this point.

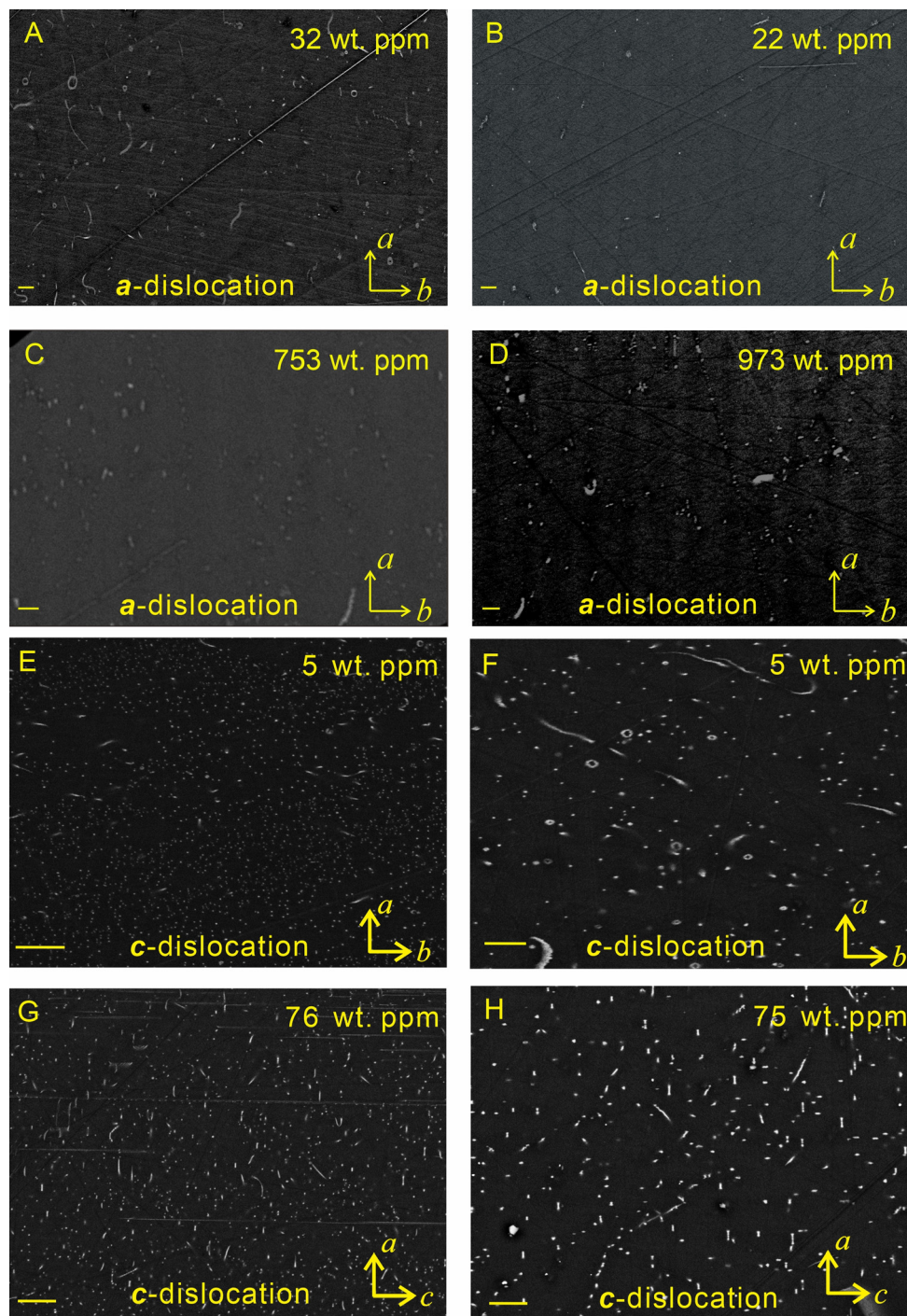


Fig. 3. Backscattered electron images of oxidation-decorated olivine. The bright spots and lines are interpreted to indicate the presence of dislocations. The scale bars denote 2 μm . The **a**-dislocation structure of sample Z1994 (A) before and (B) after annealing. The **a**-dislocation structure of sample Z1940-2 (C) before and (D) after annealing. The **c**-dislocation structure of sample Z1483 (E) before and (F) after annealing. The **c**-dislocation structure of sample Z1731 (G) before and (H) after annealing. The water contents in the samples are shown at the right corner.

No dislocations were observed in the cold compressed sample after oxidation decoration treatment (Fig. S4), which indicates that the dislocations observed in this study were produced during high-temperature deformation.

3.3. Dislocation annihilation

The slower dislocation segment limits the dislocation-creep rate in a specific slip system. The k values were therefore determined using the screw segments in the **c**-dislocations at lower water

contents (<25 wt. ppm), edge segments in the **c**-dislocations at higher water contents, and edge segments in the **a**-dislocations for the entire range of water contents. Although the dislocation density should be obtained from the sum of the apparent dislocation densities in the two directions normal to the slip plane, we measured the densities of the dominant dislocation segments because these segments have lower mobility and therefore rate-limit the creep rate of the slip system. In addition, the density change of the non-dominant dislocation segments is negligibly small because

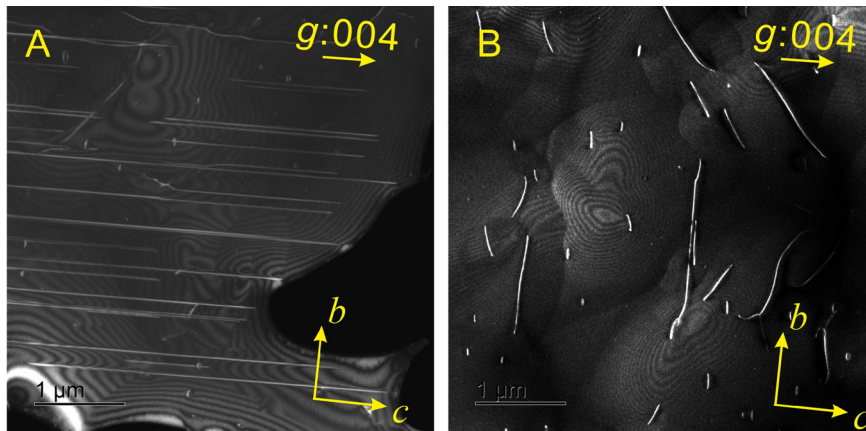


Fig. 4. TEM images showing the changes in the *c*-dislocation characteristics with (A) 7 wt. ppm and (B) 75 wt. ppm water. The screw and edge segments of the dislocations elongate in the [001] and [010] directions, respectively.

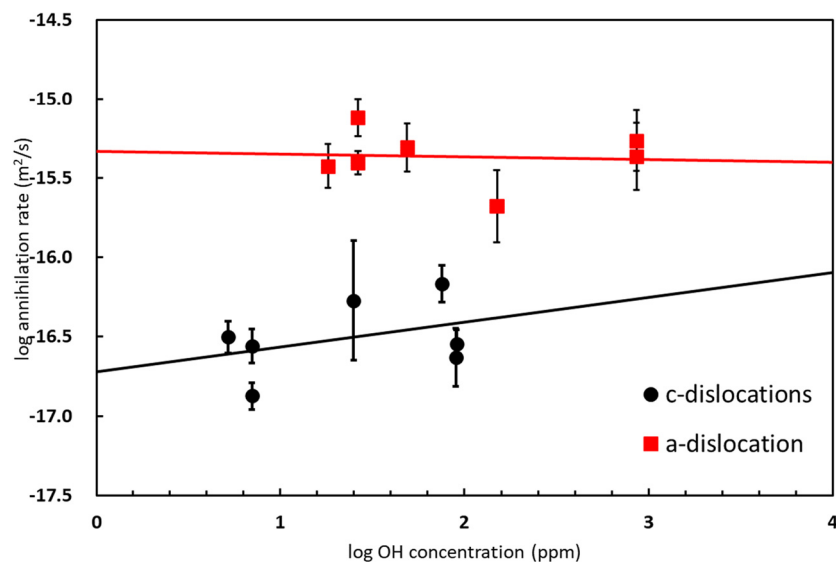


Fig. 5. Dislocation-annihilation rate coefficient (*k*) as a function of water content in olivine.

the dislocation-annihilation rate is proportional to the squared dislocation density, as shown in Eq. (1).

Non-hydrostatic conditions in a multi-anvil cell assembly can produce some new dislocations during annealing. However, the resulting dislocations in our annealing assembly have a density of less than $0.003 \mu\text{m}^{-2}$ (Rubie et al., 1993), which is negligible compared with the final dislocation density (Table 1). The newly produced dislocations during annealing were therefore omitted when calculating *k*.

The experimental conditions and results are summarized in Table 1. The details of dislocation counting are summarized in Table S2. Our calculated *k* is independent of the initial dislocation density, which indicates that the recovery follows second-order kinetics. Fitting the rate coefficients to Eq. (3) yields water-content exponents, *r*, of 0.0 ± 0.1 and 0.2 ± 0.2 for *a*- and *c*-slip, respectively (Fig. 5). The R-squared values for fitting the *a*- and *c*-slip data are 0 and 0.2, and the residual sum of squares (RSS) are 0.2 and 0.3, respectively. Because the dislocation-creep rate should be primarily proportional to dislocation mobility (Karato and Ogawa, 1982), these results suggest minimal and indistinguishable effects of water on the creep rates in these two slip-systems under low-stress and water under-saturated conditions. Note that the water-content range of the *c*-dislocation experiment is limited, i.e., 1.3 orders of magnitude. The actual uncertainty of water-content ex-

ponent of *c*-dislocation could be larger than the values obtained by the mathematic fitting, i.e., ± 0.2 .

4. Discussion

4.1. Change of dislocations structure with water content and water-content exponents

As mentioned above, the dominant segment changes from screw to edge in *c*-dislocations at ca. 25 wt. ppm with increasing water content. This fact suggests that water enhances the mobility of the screw segment more than the edge segment in *c*-dislocations (Fig. S5) because the dominant segment is always the slower one. Since the slower segment limits the overall mobility, the screw segment should be rate-limiting at water contents lower than 25 wt. ppm. Therefore, *c*-dislocations may have a higher water-content exponent than the current estimation, i.e. 0.2, in this water content range. However, since the water-content of 25 wt. ppm is the lower end of the widely accepted water-content range in the majority of the upper mantle (20–300 wt. ppm) (Dixon et al., 2004; Li et al., 2008), the *c*-dislocation mobility in the upper mantle should be limited by the edge segment, and its water-content dependence of the mobility should be similar or even smaller than given in this study. Note that the possible higher water-content de-

pendence at lower water content agrees with the results of Tielke et al. (2017, 2019).

4.2. Small effect of water on the olivine dislocation-creep rate

The water-content exponents obtained in this study are considerably smaller than those suggested by early polycrystalline-olivine deformation experiments (1.2) (Karato and Jung, 2003; Mei and Kohlstedt, 2000). The high water-content exponent obtained in those studies might have been due to the large activation volume assumed in their arguments. The activation volumes used in Mei and Kohlstedt (2000) and Karato and Jung (2003) were 34 and 14 cm³/mol, respectively. If applying the activation volume obtained in Wang et al. (2017), namely 2.5 cm³/mol, the water exponents would decrease to 0.7 and 0.5, respectively, in Mei and Kohlstedt (2000) and Karato and Jung (2003). However, these water-content exponents are still higher than the values obtained here. We also note that since Wang et al. (2017) determined the pressure dependence of dislocation mobility under dry conditions, it is not absolutely clear whether their activation volume is applicable for the present argument. Therefore, there should be another reason for the discrepancies. The oxygen fugacity in these two studies are Ni-NiO buffer conditions, which is similar to the EMOG buffer condition in this study. The Si activity was controlled by the presence of enstatite in Mei and Kohlstedt, 2000, which is the same as the present one. Therefore, the different water-content exponents cannot be explained by the chemical environment between these two studies and the present one. One possibility is that the water-content exponent is pressure dependent. The experiments from Mei and Kohlstedt (2000) and Karato and Jung (2003) were done at the pressure below 3 GPa, while ours were done at 5 GPa. The water-content exponent could decrease with increasing pressure. Another possible reason for this discrepancy might be the enhancement of grain boundary migration or sliding due to free water in their experiments because their experiments were water-saturated but ours is undersaturated (Fei et al., 2013 and Supplementary Materials, Fig. S6).

Our results generally agree with single-crystal deformation results (Girard et al., 2013; Mackwell et al., 1985; Tielke et al., 2019, 2017). Mackwell et al. (1985) indicated an average exponent of 0.2 among different slip systems. Deformation experiments on olivine single crystals with activated *a*-slip showed a zero water-content dependence within the experimental error (Girard et al., 2013), which agrees with our results. Their study also demonstrated that the stresses remained nearly constant at a constant strain rate even the water content in the olivine crystals decreased from 61 to 18 wt. ppm during the deformation experiments. Tielke et al. (2017) reported that olivine single crystals with a water content of 12 wt. ppm are 10 times weaker than dry olivine single crystals when *c*-slip is the primary creep mechanism. The water content in “dry” olivine single crystals should be less than 0.06 wt. ppm (Mackwell et al., 1985). These results lead to an upper limit of the water-content exponent of 0.4, which agrees with the present *c*-slip results. The recent result from Tielke et al. (2019) reads $r = 0.4$ and 0.2 for *a*- and *c*-slip, respectively, by assuming a stress exponent of 3.5.

The viscosity of single-crystal olivine when its strain is fully accommodated by *a*-slip or *c*-slip (η_a and η_c , respectively) can be computed as (see Supplementary Materials):

$$\eta_i = \frac{\sigma}{\dot{\epsilon}_i} = \frac{\alpha b_i^2}{B} \left(\frac{\mu}{\sigma} \right)^{2.4} \frac{\sigma}{k_i}, \quad (4)$$

under the assumption that climb motion is the rate-controlling process, where the subscript i denotes the different slip systems, B is a constant equal to 1.74×10^{-3} , α is a constant on the order of

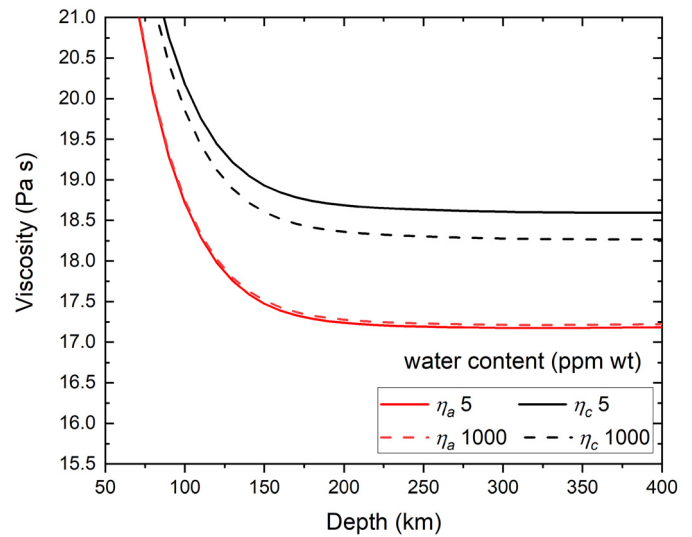


Fig. 6. Estimated olivine viscosity in the upper mantle. The viscosity of olivine is estimated from dislocation creep caused by *a*- and *c*-slip (η_a and η_c , respectively) at asthenospheric pressures, temperatures, and variable water contents (5 and 1000 wt. ppm, as shown in the legend). The temperature is along the geotherm under 70-Ma plates. The viscosity was calculated using Eq. (2) with k extrapolated from the present study. The viscosity of olivine aggregate should lie between η_a and η_c .

100, b is the length of the Burgers vector, σ is the stress, and μ is the shear modulus (80 GPa) (Bai and Kohlstedt, 1992). The k values are then corrected from our experimental conditions to asthenospheric conditions along a geotherm under 70-Ma plates (Katsura et al., 2017) using an activation energy of 400 kJ/mol (Wang et al., 2016) and activation volumes of 2.7 and 2.5 cm³/mol for the *a*- and *c*-slips, respectively (Wang et al., 2017). These calculations suggest that η_a is independent of water content, and η_c decreases by only a factor of three upon increasing the olivine water content from 5 to 1000 wt. ppm (Fig. 6). The calculations also suggest that η_a is generally lower than η_c , although the difference is small and within one order of magnitude.

The small effect of water incorporation on dislocation mobility in olivine implies that structural water in olivine may not significantly influence the viscosity of the upper mantle, which should be controlled by the viscosity of olivine aggregates as a first approximation (Hirth and Kohlstedt, 2003). Because *c*- and *a*-dislocations are considered the most and least water-sensitive dislocations, respectively (Jung and Karato, 2001; Karato et al., 2008), the viscosity variation of olivine aggregates due to water incorporation should lie between those of η_a and η_c estimated above. Namely, the water-content exponent of olivine-aggregate viscosity is expected to be between -0.1 and 0.4 . In addition, the aggregate strength has been suggested to be controlled by the strongest slip system when the strains are large (Ashby and Duval, 1985). If this is the case, the water-content exponent of η_c ($r = 0.2 \pm 0.2$) should represent that of olivine aggregate because $\eta_c > \eta_a$. Although grain-boundary sliding could be significant under asthenospheric conditions (Hansen et al., 2011; Ohuchi et al., 2015), dislocation creep plays an essential role in this process because the sliding of two adjacent grains must be accommodated by dislocation motion within a third grain at the triple junction (Ohuchi et al., 2015). A strong viscosity contrast between the lithosphere and asthenosphere is therefore difficult to produce from a difference in water content alone because water incorporation may reduce the viscosity of the asthenosphere by only less than a half order of magnitude (Fig. 6). The viscosity difference may therefore be mainly caused by the temperature effect.

4.3. Negligible effect of water on fabric transition

The present results suggest that a water-induced A- to C-type fabric transition (Karato et al., 2008) may not occur in the oceanic asthenosphere. The fabric is controlled by the weakest slip system of the dominant minerals (Lister, 1979). Our calculation shows no crossover between η_a and η_c (Fig. 6). Accordingly, A-type fabric is expected to dominate in the major parts of the asthenosphere.

The dominance of A-type over C-type fabric implies that the seismic anisotropy variation may be mainly caused by different mantle-flow directions rather than variable water contents in different regions. Under horizontal (vertical) shear, the horizontally polarized shear-wave velocity (V_{SH}) is higher (lower) than the vertically polarized shear-wave velocity (V_{SV}) in A-type fabric. Although E-type fabric could dominate in the asthenosphere under moderate water-content conditions (Katayama et al., 2004), the V_{SH}/V_{SV} anisotropy in E-type fabric is nearly identical to that in A-type fabric (Katayama et al., 2004). The $V_{SV} > V_{SH}$ anisotropy under Iceland (Gaherty, 2001) is therefore likely caused by plume upwelling. The $V_{SV} > V_{SH}$ anisotropy in broad regions under the Pacific below 300 km, whose center is located near Hawaii, could also be caused by vertical flow.

Although our results indicate that water may not cause an olivine fabric transition in the oceanic asthenosphere, other factors (e.g., pressure, stress) must be considered when interpreting the whole upper-mantle seismic anisotropy. Despite some debate (Karato et al., 2008; Wang et al., 2017), previous deformation studies (Couvry et al., 2004; Hilairet et al., 2012; Ohuchi et al., 2011; Raterron et al., 2007) have suggested a pressure-induced A- to B-type fabric transition. Because the V_{SH}/V_{SV} anisotropy in B-type fabric differs from that in A-type fabric (Jung and Karato, 2001), a change of V_{SV}/V_{SH} seismic anisotropy at depths greater than 300 km (Gung et al., 2003) could be attributed to this fabric transition. A stress-induced A- to B-type fabric transition (Jung et al., 2006) could also occur in high-stress and water-saturated regions in the upper mantle, such as subduction zones.

5. Conclusions

The present study shows that the water exponents of the dislocation-annihilation rate coefficients for the [100](010) and [001](100) slip systems are small and identical to each other within error: 0.0 ± 0.1 and 0.2 ± 0.2 , respectively. The small water-content dependences of dislocation mobility in these two slip systems indicate that water may not significantly reduce the olivine single-crystal dislocation creep rate. Assuming the strength of olivine aggregate is controlled by dislocation creep in the hardest slip system, the water-content dependence of olivine aggregate dislocation creep should be less than 0.4. In addition, an A-type to C-type water-induced fabric transition is unlikely in the majority of the asthenosphere, where stresses are low and olivine is water under-saturated. A reduction of viscosity in the major parts in the asthenosphere due to water incorporation in olivine may therefore be limited. Moreover, the variation of lateral seismic anisotropy in the asthenosphere could simply be caused by changes of mantle flow geometry rather than differing water contents in olivine. Finally, due to the scattered data points, the water-content exponent of $\dot{\epsilon}$ -dislocation is subjected to a relatively large uncertainty. Further investigation at a larger water content range may confirm the current conclusion.

CRediT authorship contribution statement

Lin Wang: Formal analysis, Investigation, Methodology, Validation, Writing – original draft. **Artem Chanyshv:** Formal analysis, Investigation, Validation. **Nobuyoshi Miyajima:** Investigation.

Takaaki Kawazoe: Investigation. **Stephan Blaha:** Investigation. **Jia Chang:** Investigation. **Tomoo Katsura:** Conceptualization, Methodology, Supervision.

Declaration of competing interest

The authors declare that they have no known competing financial interests or personal relationships that could have appeared to influence the work reported in this paper.

Data availability

All data are available in the main text or Supplementary Materials.

Acknowledgements

We thank H. Fischer and R. Njål for manufacturing the sample assembly components and sample preparation. **Funding:** This research was supported by DFG grants to T.K. (KA3434-3/1, KA3434-3/2, KA3434-7/1, KA3434-8/1, and KA3434-11/1) and by the annual budget of BGI. The TEM facility at the Bayerisches Geoinstitut is supported by DFG grant INST 91/251-1 FUGG.

Appendix A. Supplementary material

Supplementary material related to this article can be found online at <https://doi.org/10.1016/j.epsl.2021.117360>.

References

- Angel, R., Finger, L., 2011. SINGLE: a program to control single-crystal diffractometers. *J. Appl. Crystallogr.* 44, 247–251.
- Ashby, M., Duval, P., 1985. The creep of polycrystalline ice. *Cold Reg. Sci. Technol.* 11, 285–300.
- Bai, Q., Kohlstedt, D.L., 1992. High-temperature creep of olivine single crystals, 2. Dislocation structures. *Tectonophysics* 206, 1–29.
- Chopra, P.N., Paterson, M.S., 1984. The role of water in the deformation of dunite. *J. Geophys. Res.* 89, 7861–7876.
- Cordier, P., Amodeo, J., Carrez, P., 2012. Modelling the rheology of MgO under Earth's mantle pressure, temperature and strain rates. *Nature* 481, 177–180.
- Costa, F., Chakraborty, S., 2008. The effect of water on Si and O diffusion rates in olivine and implications for transport properties and processes in the upper mantle. *Phys. Earth Planet. Inter.* 166, 11–29.
- Couvry, H., Frost, D.J., Heidelbach, F., Nyilas, K., Ungar, T., Mackwell, S., Cordier, P., 2004. Shear deformation experiments of forsterite at 11 GPa–1400 °C in the multianvil apparatus. *Eur. J. Mineral.* 16, 877–889.
- Dixon, J.E., Dixon, T.H., Bell, D., Malservisi, R., 2004. Lateral variation in upper mantle viscosity: role of water. *Earth Planet. Sci. Lett.* 222, 451–467.
- Ekström, G., Dziewonski, A.M., 1998. The unique anisotropy of the Pacific upper mantle. *Nature* 394, 168–172.
- Farla, R.J.M., Kokkonen, H., Fitz Gerald, J.D., Barnhoorn, A., Faul, U.H., Jackson, I., 2011. Dislocation recovery in fine-grained polycrystalline olivine. *Phys. Chem. Miner.* 38, 363–377.
- Fei, H., Wiedenbeck, M., Yamazaki, D., Katsura, T., 2013. Small effect of water on upper-mantle rheology based on silicon self-diffusion coefficients. *Nature* 498, 213–215.
- Fei, H., Wiedenbeck, M., Yamazaki, D., Katsura, T., 2014. No effect of water on oxygen self-diffusion rate in forsterite. *J. Geophys. Res., Solid Earth* 119, 7598–7606.
- Gaherty, J.B., 2001. Seismic evidence for hotspot-induced buoyant flow beneath the Reykjanes Ridge. *Science* 293, 1645–1647.
- Girard, J., Chen, J., Raterron, P., Holyoke III, C.W., 2013. Hydrolytic weakening of olivine at mantle pressure: evidence of 100 (010) slip system softening from single-crystal deformation experiments. *Phys. Earth Planet. Inter.* 216, 12–20.
- Gose, J., Schmaedick, E., Markowitz, M., Beran, A., 2010. OH point defects in olivine from Pakistan. *Mineral. Petrol.* 99, 105–111.
- Gung, Y., Panning, M., Romanowicz, B., 2003. Global anisotropy and the thickness of continents. *Nature* 422, 707–711.
- Hansen, L.N., Zimmerman, M.E., Kohlstedt, D.L., 2011. Grain boundary sliding in San Carlos olivine: flow law parameters and crystallographic-preferred orientation. *J. Geophys. Res., Solid Earth* 116, B08201.
- Hilairet, N., Wang, Y., Sanhira, T., Merkel, S., Mei, S., 2012. Deformation of olivine under mantle conditions: an in situ high-pressure, high-temperature study using monochromatic synchrotron radiation. *J. Geophys. Res., Solid Earth* 117.

- Hirth, G., Kohlstedt, D., 2003. Rheology of the Upper Mantle and the Mantle Wedge: A View from the Experimentalists, Inside the Subduction Factory. American Geophysical Union, pp. 83–105.
- Jung, H., Karato, S.-i., 2001. Water-induced fabric transitions in olivine. *Science* 293, 1460–1463.
- Jung, H., Katayama, I., Jiang, Z., Hiraga, T., Karato, S., 2006. Effect of water and stress on the lattice-preferred orientation of olivine. *Tectonophysics* 421, 1–22.
- Karato, S.-i., Jung, H., 2003. Effects of pressure on high-temperature dislocation creep in olivine. *Philos. Mag.* 83, 401–414.
- Karato, S.-i., Jung, H., Katayama, I., Skemer, P., 2008. Geodynamic significance of seismic anisotropy of the upper mantle: new insights from laboratory studies. *Annu. Rev. Earth Planet. Sci.* 36, 59–95.
- Karato, S., Ogawa, M., 1982. High-pressure recovery of olivine: implications for creep mechanisms and creep activation volume. *Phys. Earth Planet. Inter.* 28, 102–117.
- Karato, S.I., Paterson, M.S., FitzGerald, J.D., 1986. Rheology of synthetic olivine aggregates: influence of grain size and water. *J. Geophys. Res., Solid Earth* 91, 8151–8176.
- Katayama, I., Jung, H., Karato, S.-i., 2004. New type of olivine fabric from deformation experiments at modest water content and low stress. *Geology* 32, 1045–1048.
- Katsura, T., Baba, K., Yoshino, T., Kogiso, T., 2017. Electrical conductivity of the oceanic asthenosphere and its interpretation based on laboratory measurements. *Tectonophysics* 717, 162–181.
- Kohlstedt, D.L., 2006. The role of water in high-temperature rock deformation. *Rev. Mineral. Geochem.* 62, 377–396.
- Kohlstedt, D., Keppler, H., Rubie, D., 1996. Solubility of water in the α , β and γ phases of $(\text{Mg, Fe})_2\text{SiO}_4$. *Contrib. Mineral. Petrol.* 123, 345–357.
- Kohlstedt, D., Nichols, H., Hornack, P., 1980. The effect of pressure on the rate of dislocation recovery in olivine. *J. Geophys. Res., Solid Earth (1978–2012)* 85, 3122–3130.
- Li, Z.X.A., Lee, C.T.A., Peslier, A.H., Lenardic, A., Mackwell, S.J., 2008. Water contents in mantle xenoliths from the Colorado Plateau and vicinity: implications for the mantle rheology and hydration-induced thinning of continental lithosphere. *J. Geophys. Res., Solid Earth* 113.
- Lister, G., 1979. Fabric transitions in plastically deformed quartzites: competition between basal, prism and rhomb systems. *Bull. Minéral.* 102, 232–241.
- Mackwell, S.J., Kohlstedt, D.L., Paterson, M.S., 1985. The role of water in the deformation of olivine single-crystals. *J. Geophys. Res., Solid Earth Planets* 90, 1319–1333.
- Masuti, S., Karato, S.-i., Girard, J., Barbot, S.D., 2019. Anisotropic high-temperature creep in hydrous olivine single crystals and its geodynamic implications. *Phys. Earth Planet. Inter.* 290, 1–9.
- Mei, S., Kohlstedt, D.L., 2000. Influence of water on plastic deformation of olivine aggregates 2. Dislocation creep regime. *J. Geophys. Res., Solid Earth* 105, 21471–21481.
- Montagner, J.-P., Guillot, L., 2002. Seismic anisotropy and global geodynamics. *Rev. Mineral. Geochem.* 51, 353–385.
- Ohuchi, T., Kawazoe, T., Higo, Y., Funakoshi, K.-i., Suzuki, A., Kikegawa, T., Irifune, T., 2015. Dislocation-accommodated grain boundary sliding as the major deformation mechanism of olivine in the Earth's upper mantle. *Sci. Adv.* 1, e1500360.
- Ohuchi, T., Kawazoe, T., Nishihara, Y., Nishiyama, N., Irifune, T., 2011. High pressure and temperature fabric transitions in olivine and variations in upper mantle seismic anisotropy. *Earth Planet. Sci. Lett.* 304, 55–63.
- Paterson, M., 1982. The determination of hydroxyl by infrared absorption in quartz, silicate glasses, and similar materials. *Bull. Soc. Fr. Mineral.* 105, 20–29.
- Raterron, P., Chen, J., Li, L., Weidner, D., Cordier, P., 2007. Pressure-induced slip-system transition in forsterite: single-crystal rheological properties at mantle pressure and temperature. *Am. Mineral.* 92, 1436–1445.
- Rubie, D., Karato, S., Yan, H., O'Neill, H.S.C., 1993. Low differential stress and controlled chemical environment in multianvil high-pressure experiments. *Phys. Chem. Miner.* 20, 315–322.
- Sternai, P., Avouac, J.-P., Jolivet, L., Faccenna, C., Gerya, T., Becker, T.W., Menant, A., 2016. On the influence of the asthenospheric flow on the tectonics and topography at a collision-subduction transition zones: comparison with the eastern Tibetan margin. *J. Geodyn.* 100, 184–197.
- Tielke, J., Mecklenburgh, J., Mariani, E., Wheeler, J., 2019. The influence of water on the strength of olivine dislocation slip systems. *J. Geophys. Res., Solid Earth* 124, 6542–6559.
- Tielke, J.A., Zimmerman, M.E., Kohlstedt, D.L., 2017. Hydrolytic weakening in olivine single crystals. *J. Geophys. Res., Solid Earth* 122, 3465–3479.
- Toriumi, M., Karato, S.-i., 1978. Experimental studies on the recovery process of deformed olivines and the mechanical state of the upper mantle. *Tectonophysics* 49, 79–95.
- Visser, K., Trampert, J., Lebedev, S., Kennett, B.L.N., 2008. Probability of radial anisotropy in the deep mantle. *Earth Planet. Sci. Lett.* 270, 241–250.
- Wang, L., Blaha, S., Kawazoe, T., Miyajima, N., Katsura, T., 2017. Identical activation volumes of dislocation mobility in the [100](010) and [001](010) slip systems in natural olivine. *Geophys. Res. Lett.* 44, 2687–2692.
- Wang, L., Blaha, S., Pintér, Z., Farla, R., Kawazoe, T., Miyajima, N., Michibayashi, K., Katsura, T., 2016. Temperature dependence of [100](010) and [001](010) dislocation mobility in natural olivine. *Earth Planet. Sci. Lett.* 441, 81–90.